J|A|C|S ARTICLES

Published on Web 04/01/2010

Multiple Nonstoichiometric Phases with Discrete Composition Ranges in the $CaAu_5-CaAu_4Bi-BiAu_2$ System. A Case Study of the Chemistry of Spinodal Decomposition

Qisheng Lin and John D. Corbett*

Ames Laboratory, USDOE, and Department of Chemistry, Iowa State University, Ames, Iowa 50011

Received January 11, 2010; E-mail: jcorbett@iastate.edu; jdc@ameslab.gov

Abstract: Synthetic explorations in the $CaAu_5-CaAu_4Bi-BiAu_2$ system at 400 °C reveal five separate solid solution regions that show three distinct substitution patterns in the $CaAu_5$ parent: (**I**) $CaAu_4(Au_{1-m}Bi_m)$ with $0 \le m \le 0.15(1)$, (**II**) $0.33(1) \le m \le 0.64(1)$, (**III**) $0.85(4) \le m \le 0.90(2)$; (**IV**) $(Ca_{1-r}Au_r)Au_4(Bi_{1-s}Au_s)$ with $0 \le r \le 0.39(1)$ and $0 \le s \le 0.12(2)$; (**V**) $(Ca_{1-p-q}Au_pBi_q)Au_4Bi$ with $0.09(2) \le p \le 0.13(1)$ and $0.31(2) \le q \le 0.72(4)$. Single crystal X-ray studies establish that all of these phase regions have common cubic symmetry $F\bar{4}3m$ and that their structures ($MgCu_4Sn$-type, an ordered derivative of $MgCu_2$) all feature three-dimensional networks of Au_4 tetrahedra, in which the truncated tetrahedra are centered and capped by Ca/Au, Au/Bi, or Ca/Au/Bi mixtures to give 16-atom Friauf polyhedra. TB-LMTO-ASA and -COHP calculations also reveal that direct interactions between Ca−Au and Ca−Bi pairs of atoms are relatively weak and that the Bi−Au interactions in the unstable ideal $CaAu_4Bi$ are antibonding in character at E_F but that their bonding is optimized at ±1 *e*. Compositions between the five nonstoichiometric phases appear to undergo spinodal decompositions. The last phenomenon has been confirmed by HRTEM, STEM-HAADF, EPMA, and XRD studies of the nominal composition $CaAu_{4.25}Bi_{0.75}$. Its DTA analyses suggest that the phases resulting from spinodal decomposition have nearly the same melting point (~807 °C), as expected, and that they are interconvertible through peritectic reactions at ~717 °C.

Introduction

Spinodal decomposition affords a very useful phase transition mechanism by which markedly fine-grained coherent structures can form naturally on micro- or nanoscales.[1−3] This phenomenon occurs under the thermodynamic condition that the second derivative of the free energy of mixing for a pair of partially miscible components is negative,[4] i.e., $\partial G^2/\partial X^2 < 0$ (X is the mole fraction). On the contrary, the more classical nucleation and growth processes occur when $\partial G^2/\partial X^2$ is positive. According to the Gibbs criteria for phase stabilities,[5] a spinodal decomposition is a phase transition that is small in degree (composition change) but large in extent (size), whereas the more common nucleation process is large in degree but small in extent. In contrast to nucleation and growth processes that require thermodynamic activation, there is no thermodynamic barrier for a spinodal process. The latter is determined solely by diffusion processes.

Spinodal decomposition, a first-order (or discontinuous) phase transition, always causes a single (unstable) phase to separate into a spinodal pair with the *same structure but slightly different compositions* after cooling below a certain temperature.[6] Translated into a more chemist-friendly language, this statement means that spinodal decomposition occurs below a certain temperature only when the following minimal conditions are met: (1) the product consists of a pair of isostructural compounds or solid solutions that have very similar elemental proportions and (2) both compositions are stable but their average is not. Spinodal phenomena have been found in diverse intermetallic or alloy systems,[1,2] polymer blends,[7] oxides,[8] and certain semiconductors.[9] A majority of studies on spinodal decomposition have been theoretical in nature, including computer simulations, and others have focused on applications of known systems. However, the discovery of a new spinodal system is relatively infrequent. Spinodal systems have been developed for numerous practical applications such as ultrahigh-strength steels, optical recording media, and magnetic alloys.[1,2] Recently, spinodal decomposition has also been investigated as a promising means to enhance the energy conversion efficiency of thermoelectric materials by increasing the thermal (phonon) scattering.[10]

(1) Miyazaki, T. *Process., Prop. Appl. Met. Ceram. Mater., Proc. Int. Conf.* **1992**, *1*, 13.
(2) Ditchek, B.; Schwartz, L. H. *Annu. Rev. Mater. Sci.* **1979**, *9*, 219.
(3) Favvas, E. P.; Mitropoulos, A. C. *J. Eng. Sci. Tech. Rev.* **2008**, *1*, 25.
(4) Cahn, J. W. *J. Chem. Phys.* **1965**, *42*, 93.
(5) Gibbs, J. W. *Scientific Papers of J. Willard Gibbs*; Dover: New York, 1961; Vol. 2, pp 105−252.
(6) Toleìdano, J.-C.; Toleìdano, P. *The Landau theory of phase transitions: application to structural, incommensurate, magnetic, and liquid crystal systems*; World Scientific: Singapore; Teaneck, NJ, 1987; p 451.
(7) Wacharawichanant, S.; Thongyai, S.; Tanodekaew, S.; Higgins, J. S.; Clarke, N. *Polymer* **2004**, *45*, 2201.
(8) SanSoucie, M.; Hyers, R. W. *Ceram. Trans.* **2005**, *164*, 111.
(9) Jaw, D. H.; Chang, J. R.; Su, Y. K. *Appl. Phys. Lett.* **2003**, *82*, 3883.
(10) Androulakis, J.; Lin, C.-H.; Kong, H.-J.; Uher, C.; Wu, C.-I.; Hogan, T.; Cook, B. A.; Caillat, T.; Paraskevopoulos, K. M.; Kanatzidis, M. G. *J. Am. Chem. Soc.* **2007**, *129*, 9780.

10.1021/ja100250d

Here we report the discovery of several separate solid solution regions in the $CaAu_5-CaAu_4Bi-BiAu_2$ system with evidence for spinodal decompositions in regions between them. The ternary phase $CaAu_{\sim 4}Bi$ was unexpectedly encountered in our continuing search for quasicrystals (QCs) and approximants (ACs)[11−13] in the Ca−Au−Bi system, which followed on our explorations and developments of these in the Ca−Au−Ge and Ca−Au−Sn systems.[14] Ideal $CaAu_4Bi$ is an ordered ternary derivative of $CaAu_5$ ($F\bar{4}3m$)[15] both of which contain a three-dimensional network of vertex-sharing Au_4 tetrahedra, an arrangement that is also found in $BiAu_2$ ($Fd\bar{3}m$).[16] These relationships are clearer according to the rearranged representations $CaAu_4Au$ (= $CaAu_5$), $BiAu_4Bi$ (= $BiAu_2$), and $CaAu_4Bi$, in which, for consistency, the elements at the Wyckoff 4*a* and 4*c* positions are always listed first and last, with the 16*e* Au site that generates the common $_\infty^3[Au_4]$ network in the middle. (In this case, the symmetry of $BiAu_2$ is transformed to $Fd\bar{3}m$.) The corresponding ternary system is remarkable not only for the closely related structural motifs in all three terminal compounds, a rare case, but also for the unusual opportunity to observe multiple spinodal systems. The experience derived from this system may shed new light on the design and chemical tuning of other related spinodal systems.

Experimental Section

Syntheses. The starting materials were high purity elements: Ca dendrites, Au particles, and Bi pieces (all >99.99%, Alfa-Aesar). These elements (~400 mg in total) were weighed in a N_2-filled glovebox (H_2O < 0.1 ppm vol.) and weld-sealed into Ta containers under Ar, which were in turn enclosed in evacuated SiO_2 jackets ($<10^{-5}$ Torr) to avoid oxidation of the metal containers by air at higher temperatures.

$CaAu_{\sim 4}Bi$ was first encountered as the major product (~80%) from an exploratory reaction of nominal $CaAu_{4.5}Bi_{1.5}$ that had been heated to 850 °C, held at this temperature for 12 h, cooled to 400 °C at a rate of 5 °C/h, annealed there for 1 week, and then quenched in water. Single crystal X-ray diffraction studies established it as $CaAu_4Bi$ ($MgCu_4Sn$-type[17]). (Note: its actual composition is slightly off stoichiometry according to EDS, so in the text we use $CaAu_{\sim 4}Bi$ to represent all nonstoichiometric phases with this atom site distribution if the compositions are not particularly specified.) This phase can be considered as a ternary derivative of both $CaAu_5$ ($F\bar{4}3m$, $AuBe_5$-type[15]) and $BiAu_2$ ($Fd\bar{3}m$, $MgCu_2$-type[16]). Next, three batches of reactions that included the three terminal phases, (a) $CaAu_4(Au_{1-x}Bi_x)$ (x = 0, 0.25, 0.5, 0.75, 1), (b) $(Ca_{1-y}Bi_y)Au_4Bi$ (y = 0.4, 0.8, 1), and (c) $(Ca_zBi_{1-z})Au_4(Au_zBi_{1-z})$ (z = 0.33, 0.67) were carried out under the following profile: heat to 850 °C and dwell there for 12 h, quench in water, and then anneal at 400 °C for 1 week before quenching the containers and contents in water. These three ranges actually represent solid solution regions, the compositions of which are located on the lines defined by $CaAu_5-CaAu_4Bi$, $CaAu_4Bi-BiAu_2$, and $CaAu_5-BiAu_2$, respectively. Four additional reactions of $Ca_{0.6}Au_{4.33}Bi_{1.07}$, $CaAu_{3.75}Bi_{1.25}$, $Ca_{1.4}Au_4Bi_{0.6}$, and $CaAu_{3.5}Bi_{1.5}$ were also carried out; the first falls within the $CaAu_5-CaAu_4Bi-BiAu_2$ triangle, and the other three lie beyond that region.

Later, an arc melting route was applied for some selected compositions (x = 0 and 1; y = 0.5, 1; z = 0.5). The arc-melted samples (each ~1.0 g, with weight losses <1.0%) were enclosed in the Ta container/SiO_2 jacket combinations and annealed at selected temperatures: 300 °C for a week for $BiAu_2$ (y = 1) and 760 °C for a week for the others. A second arc-melted $CaAu_4Bi$ (x = 1) sample was also annealed at 650 °C for a week, as directed by DTA results (below). These reactions generally resulted in high yields of target phases. The arc melting route also eliminates traces of a $Ta_{1-x}Au_x$ impurity, which was observed after reactions of samples with Au > ~70 at. % in the Ta containers that were first heated at 850 °C.

X-ray Diffraction. Powder X-ray diffraction data were collected on a Huber 670 Guinier powder camera equipped with an area detector and Cu Kα_1 radiation (λ = 1.540 598 Å) that had been calibrated with standard Si (NIST SRM 640b). Phase identities and relative volume percentages were checked with the aid of PowderCell,[18] and the lattice parameters were refined by UnitCell.[19] In most cases, the powder patterns were dominated by reflection peaks that were doublets (see later Figure 1), but they were clearly not superstructure reflections according to single crystal results. On the contrary, they could all be separately indexed in terms of two similar cubic unit cells. Table S1 in the Supporting Information gives the refined lattice parameters of the cubic products of the 17 reactions listed above.

Single crystal X-ray diffraction studies were performed on a Bruker APEX CCD diffractometer equipped with graphite-monochromatized Mo Kα (λ = 0.710 69 Å) radiation. Intensity data were collected from several crystals ~20−30 μm on edge at room temperature with an ω scan mode within θ = ~1.5°−28° and exposures of 10−30 s/frame. Data integration, Lorentz polarization, empirical absorption, and other corrections were made by SAINT and SADABS subprograms that are included in the SMART software package.[20] In all cases, acentric symmetry was suggested according to statistical $|E^2 - 1|$ values except for $BiAu_2$.[21] Full-matrix least-squares refinements on F_o^2 were performed with the aid of the SHELXTL v 6.1 program.[22] Table 1 gives some crystal and refinement data for crystals **1**−**5**, and Table 2, the resulting atomic parameters and isotropic displacement parameters. A list of important interatomic distances (Table S2) and other detailed structural information (CIF outputs) are in the Supporting Information. Single crystals of adequate size could be found after numerous synthesis and annealing reactions.

In structural refinements, the atomic positions for $CaAu_5$[15] were used as the initial structural model, except that Au at the Wyckoff 4*c* site was replaced by Bi or Bi/Au. For crystals **1**−**3**, refinements always resulted in larger displacement parameters for atoms in the Wyckoff 4*c* site (~0.019 Å^2) than in other two (~0.011 Å^2), suggesting mixed occupancies of Bi and a lighter element (Au or Ca) at this point. However, the true elemental proportions could only be well established with the aid of EDS data because Au and Bi have similar X-ray scattering factors. Otherwise, mixtures of dominant Bi (or Au) with minor Ca were always resolved in refinements. Likewise, least-squares refinements for crystals **4** and **5** suggested Ca/Bi mixtures at the Wyckoff 4*c* site despite the fact that EDS analyses (Table 1) suggested that this site also contained small amounts of Au, ~9(2) to 13(1) at. %. That is, the Wyckoff 4*c* site in **4** and **5** is occupied by Ca/Au/Bi mixtures. For simplicity however, the results for only the major Ca/Bi components are reported in the text. The Flack parameters all refined to zero, indicating that absolute structures had been established.

Elemental Analyses. Elemental analyses were made with the aid of JEOL JXA-8200 SuperProbe, equipped with a WD/ED

(11) Lin, Q.; Corbett, J. D. *Struct. Bonding (Berlin)* **2009**, *133*, 1.
(12) Lin, Q.; Corbett, J. D. *Inorg. Chem.* **2008**, *47*, 7651.
(13) Lin, Q.; Corbett, J. D. *J. Am. Chem. Soc.* **2007**, *129*, 6789.
(14) Lin, Q.; Corbett, J. D. Unpublished results.
(15) Raub, C. J.; Hamilton, D. C. *J. Less-Common Met.* **1964**, *6*, 486.
(16) Jurriaanse, T. *Z. Kristallogr.* **1935**, *90*, 322.
(17) Osamura, K.; Murakami, Y. *J. Less-Comm. Met.* **1978**, *60*, 311.
(18) Kraus, W.; Nolze, G. *J. Appl. Crystallogr.* **1996**, *29*, 301.
(19) Holland, T. J. B.; Redfer, S. A. T. *Miner. Mag.* **1997**, *61*, 65.
(20) *SMART*; Bruker AXS, Inc.: Madison, WI, 1996.
(21) The $BiAu_2$ structure was solved in 1935 from a powder data set for the Maldonite mineral [a = 7.958(2) Å].[16] For comparison, we synthesized a single crystal and refined its structure. Our results confirm that $BiAu_2$ crystallizes in $Fd3m$, a = 7.9606(4) Å, with Bi and Au fully occupying the special Wyckoff 8*a* (0, 0, 0) and 16*d* (5/8, 5/8, 5/8) positions, respectively (R1 = 0.0216, wR2 = 0.0461).
(22) *SHELXTL*; Bruker AXS, Inc.: Madison, WI, 2000.

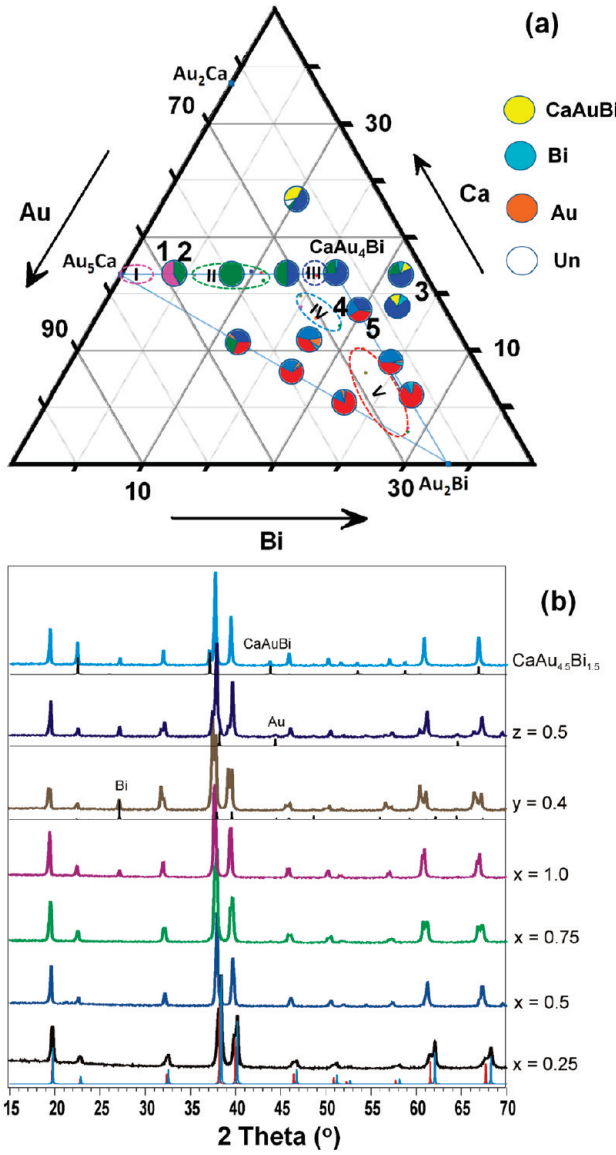

Figure 1. (a) Estimated solution regions (dashed color ovals) and product distributions (shaded pies, same color code as ovals) for reactions in the $CaAu_5$−$CaAu_4Bi$−$BiAu_2$ system at 400 °C. Numbers **1**−**5** denote products for which single crystal structures are presented in the text. (b) Powder patterns for representative annealed products (Table S1) that show single or double peaks for the dominant phases. For convenience, simulated powder patterns (bottom) from single crystal data for $CaAu_{4.75}Bi_{0.25}$ (**1** and **2**, red and blue) and locations of Au, Bi, and CaAuBi impurity lines (marked) are given as guides for phase analyses.

combined electron probe microanalyzer (EPMA). The combination of wavelength-dispersive (WDS) and energy-dispersive (EDS) X-ray spectrometers assures the most efficient and accurate analyses.[23,24] The air-stable samples were mounted in epoxy and carefully polished to avoid possible influences of sample tilting.

Generally, secondary electron images (SEI) were first obtained to distinguish phase distributions (if present) in terms of different darknesses; then measurements were made to gain an average elemental proportion for each region. However, spinodal decompositions generate spinodal pairs with fairly close compositions that are indistinguishable in SEI images. But contour maps of characteristic electron emission counts for each element (that are proportional to concentration) over each defined region (matrix) can illuminate such small changes. In our measurements, electron counts were collected on a 1 μm × 1 μm grid of randomly selected areas for nominal $CaAu_4Bi$ (400 × 550 μm^2) and $CaAu_{4.25}Bi_{0.75}$ (100 × 100 μm^2), with successive 0.4 s exposures for each grid point. These gave sufficient data to plot contour maps in which regions with slightly different compositions could be distinguished.

Microscopy Analyses. Scanning transmission electron microscopy (STEM)[25] was utilized to give direct evidence for a spinodal decomposition process. In STEM, a very small, convergent electron beam (~0.13 nm) is scanned over a defined area of a thin sample. At each spot, the generated signals are simultaneously recorded by selected detectors to build up a distribution image. Furthermore, such beams can be used to gain highly localized analyses from specimens in analytical TEM (e.g., EDS). Combinations of STEM with different detectors, e.g., bright field (BF), angular dark field (ADF), and high-angle ADF (HAADF) detectors, and with different analytical methods can accordingly be powerful tools. For example, BF-STEM studies can do an excellent job of defining crystalline areas, defects and grain boundaries, particle sizes, and phase analyses, whereas HAADF-STEM data are superb in the detection of small clusters or even single atoms of a heavy metal in a matrix of light elements (Z-contrast) and for direct visualization of structures and defects. In our experiments, a sample from nominal $CaAu_{4.25}Bi_{0.75}$, close to the center of the fitted spinodal decomposition curve (below), was selected for HAADF-STEM analyses. The sample was mechanically polished to approximately a 50−100 nm thickness before measurement.

Thermal Analyses. The thermal behaviors of several samples were studied via DTA analyses. All measurements were carried out in alumina containers with the aid of a PerkinElmer Differential Thermal Analyzer (DTA-7). Samples of ~30−90 mg were typically heated under Ar to 1000 °C at a rate of 10 °C/min and then cooled to 300 °C at the same rate. XRD patterns pre- and post-DTA scanning were also recorded.

Magnetic Susceptibility and Resistivity. Temperature-dependent magnetic susceptibility measurements were performed on a Quantum Design PPMS system during which the magnetic field was held at 10 K Oe as the temperature was varied from 4 to 300 K. A standard four-probe DC method was used to measure the resistivities of hard polycrystalline pieces over 4−300 K.

Electronic Structure Calculations. The calculations on ideal $CaAu_4Bi$ were performed by means of the self-consistent, tight-binding, linear-muffin-tin-orbital (LMTO) method in the local density (LDA) and atomic sphere (ASA) approximations, within the framework of the DFT method.[26−29] The ASA radii for Ca, Au, and Bi were automatically scaled with a maximal overlap restriction of 16%, and no interstitial spheres were necessary. All atomic spheres had reasonable radii: 3.64, 2.95, and 3.62 Å for Ca, Au, and Bi, respectively. Reciprocal space integrations were carried out using the tetrahedron method. The basis sets for Ca included 3*d*, 4*s*, and 4*p*; for Au, 6*s*, 6*p*, and 5*d*; and for Bi, 6*s* and 6*p* orbitals. Down-folding techniques[30] were applied for Ca 4*p*, Au 4*f*, and Bi 6*d* orbitals. Scalar relativistic effects were included in the calculations. Crystal orbital Hamilton population (-COHP)

(23) Reed, S. J. B. *Electron Microprobe Analyses*, 2nd ed.; Cambridge University Press: New York, 1993; p 326.
(24) Reed, S. J. B. *Electron Microprobe Analysis and Scanning Electron Microscopy in Geology*, 2nd ed.; Cambridge University Press: Cambridge, 2005; p 192.
(25) Frank, J. *Electron Tomography: Three-Dimensional Imaging with the Transmission Electron Microscope*; Plenum Press: New York; London, 1992.
(26) Tank, R.; Jepsen, O.; Burkhardt, A.; Andersen, O. K. *TB-LMTO-ASA Program*, vers. 4.7; Max-Planck Institut für Festkörperforschung: Stuttgart, Germany, 1994.
(27) Shriver, H. L. *The LMTO Method*; Springer-Verlag: Berlin, Germany, 1984.
(28) Jepsen, O.; Snob, M. *Linearized Band Structure Methods in Electronic Band-Structure and its Applications, Springer Lecture Note*; Springer Verlag: Berlin, Germany, 1987.
(29) Anderson, O. K.; Jepsen, O. *Phys. Rev. Lett.* **1984**, *53*, 2571.
(30) Lambrecht, W. R. L.; Andersen, O. K. *Phys. Rev. B* **1986**, *34*, 2439.

Table 1. Data Collection and Refinements Results for Five Single Crystals[a]

ID	1	2	3	4	5
Composition[b]	$CaAu_4[Au_{0.85(1)}Bi_{0.15(1)}]$	$CaAu_4[Au_{0.67(1)}Bi_{0.33(1)}]$	$CaAu_4[Au_{0.09(1)}Bi_{0.91(1)}]$	$BiAu_4[Ca_{0.80(1)}Bi_{0.20(1)}]$	$BiAu_4[Ca_{0.68(1)}Bi_{0.32(1)}]$
EDS compn.	$CaAu_{4.85(1)}Bi_{0.15(1)}$	$CaAu_{4.67(1)}Bi_{0.33(1)}$	$CaAu_{4.09(1)}Bi_{0.91(1)}$	$Ca_{0.75(3)}Au_{4.16(2)}Bi_{1.09(2)}$	$Ca_{0.68(3)}Au_{4.09(1)}Bi_{1.22(3)}$
f.w.	1026.71	1028.88	1035.84	1069.86	1091.40
Space group, Z	$F\bar{4}3m$, 4	$F\bar{4}3m$, 4	$F\bar{4}3m$, 4	$F\bar{4}3m$, 4	$F\bar{4}3m$, 4
Unit cell (Å)	7.7646(2)	7.8246(2)	7.9199(2)	7.9046(2)	7.9505(2)
Vol. (Å^3)	468.12(2)	479.06(2)	496.77(2)	493.90(2)	502.55(2)
d_{cal} (g/cm^3)	14.57	14.27	13.85	14.39	14.43
Abs. coeff. (mm^{-1})	157.98	155.47	153.34	161.47	163.01
Refl. coll./R(int)	710/0.0421	760/0.0344	1092/0.0363	775/0.0536	736/0.0562
Ind. ref./res./para.	83/0/8	86/0/8	88/0/8	88/0/8	85/0/8
GOF on F^2	1.240	1.116	1.134	1.137	1.162
R1/wR2 [$I > 2\sigma(I)$]	0.0200/0.0414	0.0174/0.0348	0.0136/0.0332	0.0169/0.0384	0.0234/0.0457
[all data]	0.0210/0.0417	0.0174/0.0348	0.0136/0.0332	0.0169/0.0384	0.0238/0.0461
Abs. struct. Para.	0.0(5)	0.0(8)	0.00(7)	0.0(1)	0.0(2)
peak/hole (e•Å^{-3})	1.623/−1.453	1.177/−1.368	1.561/−1.868	1.770/−1.210	1.571/−2.352

[a] Crystals **1** and **2** are from reaction of nominal $CaAu_{4.75}Bi_{0.25}$, **4** and **5** are from nominal $Ca_{0.6}Au_4Bi_{1.4}$, and **3** is from nominal $CaAu_{3.75}Bi_{1.25}$. [b] For clarity, formulas are listed in the order of compositions in the Wyckoff 4*a*, 16*e*, and 4*c* sites.

Table 2. Atomic Coordinates and Equivalent Isotropic Displacement Parameters for Crystals **1**−**5**

Crystal	Atom	Wyck.	Occ.[a]	*x*	*y*	*z*	Ueq (Å^2)
1	Ca	4*a*		0	0	0	0.011(2)
	Au	16*e*		0.6248(1)	*x*	*x*	0.011(1)
	Au/Bi	4*c*	0.85/0.15(1)	1/4	1/4	1/4	0.019(1)
2	Ca	4*a*		0	0	0	0.013(2)
	Au	16*e*		0.6249(1)	*x*	*x*	0.012(1)
	Au/Bi	4*c*	0.67/0.33(1)	1/4	1/4	1/4	0.015(1)
3	Ca	4*a*		0	0	0	0.009(1)
	Au	16*e*		0.6254(1)	*x*	*x*	0.010(1)
	Au/Bi	4*c*	0.10/0.90(1)	1/4	1/4	1/4	0.012(1)
4	Bi	4*a*		0	0	0	0.011(1)
	Au	16*e*		0.6248(1)	*x*	*x*	0.010(1)
	Ca/Bi	4*c*	0.80/0.20(1)	1/4	1/4	1/4	0.016(2)
5	Bi	4*a*		0	0	0	0.016(1)
	Au	16*e*		6253(1)	*x*	*x*	0.015(1)
	Ca/Bi	4*c*	0.68/0.32(1)	1/4	1/4	1/4	0.013(2)

[a] Bi/Au occupancies of 4c in crystals **1**−**3** were fixed according to corresponding EDS data.

analyses[31,32] were performed to gain insight into the bonding (population) properties.

Results and Discussion

Phase Analyses and Phase Relationships. Figure 1 shows (a) the phase distributions of most products (color-coded pies) together with (b) powder patterns for certain annealed samples in a select region of the Ca−Au−Bi system. As can be seen, diffraction peaks of ternary target compositions are relatively sharp but often split into two, more clearly at larger 2θ angles. These doublets do not originate from a single superstructure, but they can be indexed in terms of pairs of isostructural cubic phases with similar lattice parameters. (These are listed in Table S1 along with the composition variables (x, y, z) and sources of single crystals studied (bold numbers).) The structures of two such pairs of crystals (**1** and **2** from $x = 0.25$, **4** and **5** from $y = 0.4$) were refined with the aid of single crystal diffraction. These special relationships arise from the unusual pairwise compositions that are generated in a spinodal decomposition, the nature of which will be discussed later. In contrast, comparable peaks do not split for some other starting compositions (Table S1). For example, the powder pattern for nominal $CaAu_{4.5}Bi_{0.5}$ (Figure 1b) is almost a single phase, as also supported by EDS data ($Ca_{1.04(2)}Au_{4.48(3)}Bi_{0.48(3)}$). Also, there are no clear signs (doublets, shoulders, broadened peaks, etc.) around powder diffraction peaks from cubic ~$CaAu_4Bi$-type phases in annealed products from nominal $CaAu_{4.5}Bi_{1.5}$ (Figure 1b) and, farther away, for $Ca_{1.4}Au_4Bi_{0.6}$ and $CaAu_{3.5}Bi_{1.5}$ (Figure S1).

Figure 2 illustrates the variations of refined cubic lattice constants as a function of the starting compositions. Some compositions may yield two or three lattice parameters because multiple $CaAu_{\sim 4}Bi$ phases exist, as indicated by powder patterns. These cell constants locate in five subgroups: (**I**) 7.7292(3)−7.7646(2) Å; (**II**) 7.8124(2)−7.8982(2) Å; (**III**) 7.9006(3)−7.9199 (2) Å; (**IV**) 7.8620(2)−7.8789(3) Å; (**V**) 7.9514(2)−7.9569(2) Å for the samples investigated (Table S1), all of which had previously been equilibrated at 400 °C for 1 week. Actually, these lattice parameter groups correspond to those of five homogeneous regions (below) as represented by dashed outlines in Figure 1a. (Note: *the regions are simply drawn as ovals to include the corresponding EDS data. The actual phase boundaries may vary and may be larger*.) Although lattice parameters of **IV** fall within the range of **II**, they are not grouped together because EDS results indicate that they have distinctly different elemental proportions (below).

According to EDS analyses, the compositions of these five nonstoichiometric regions can be represented with three formula types with discontinuous composition ranges between them. Regions **I**−**III** have the same formula type $CaAu_4(Au_{1-m}Bi_m)$

(31) Dronskowski, R.; Blöch, P. *J. Phys. Chem.* **1993**, *97*, 8617.
(32) Dronskowski, R. *Computational Chemistry of Solid State Materials: A Guide for Materials Scientists, Chemists, Physicists and others*; Wiley-VCH: Weinheim, 2005; p 294.

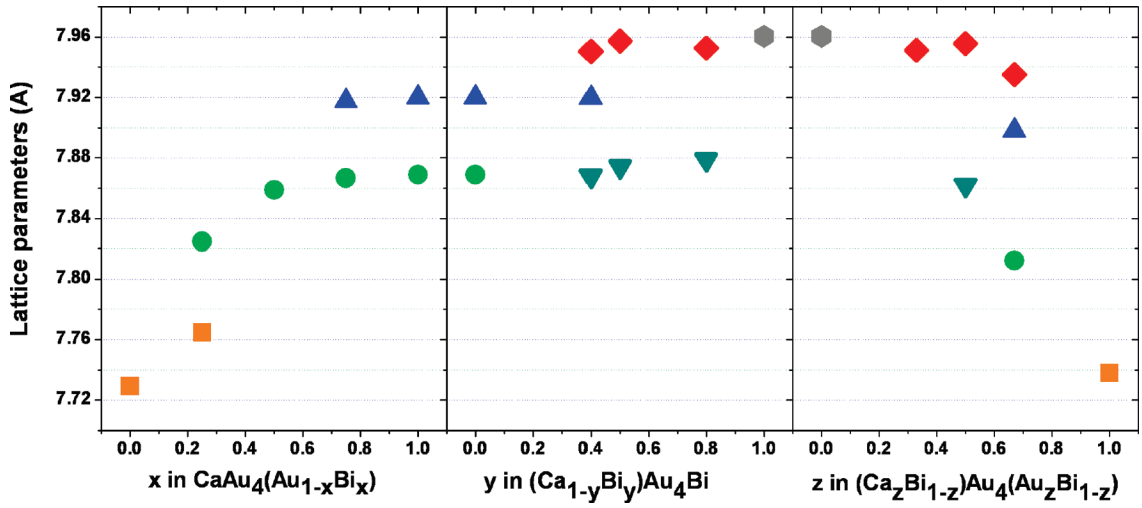

Figure 2. Variations of lattice parameters for target ~$CaAu_4Bi$ phases (including spinodal pairs) as a function of loaded compositions. The color codes are same as those in Figure 1a.

for the section studied, with $0 \le m \le 0.15(1)$ (**I**), $0.34(6) \le m \le 0.64(1)$ (**II**), and $0.85(4) \le m \le 0.90(2)$ (**III**). These can be viewed as discrete phase regions generated by substitution of Bi for Au at the Wyckoff *4c* site in $CaAu_5$. (As mentioned above, we always list occupancies of the elements in the order of theWyckoff 4*a*, 16*e*, and 4*c* sites.) As shown in Figure 2, lattice parameters increase as *m* increases because Bi has a larger effective atomic size than Au. Region **IV** can be represented by $(Ca_{1-r}Au_r)Au_4(Bi_{1-s}Au_s)$ with $0 \le r \le 0.39(1)$, $0 \le s \le 0.12(2)$ for the samples studied. Here, some Au is found in both 4*a* and *4c* sites, resulting in Ca/Au and Bi/Au mixtures, respectively, and these compositions can be considered as solid solutions of Au in the ideal solvent $CaAu_4Bi$. In contrast, region **V** can be described as $(Ca_{1-p-q}Au_pBi_q)Au_4Bi$, with $0.09(2) \le p \le 0.13(1)$ and $0.31(2) \le q \le 0.72(4)$ for the samples investigated. The last family can be considered as solutions of solutes Ca and Au in solvent $BiAu_2$ (= $BiAu_4Bi$). Of the three formula families defined, the last has the highest Bi content and the largest lattice parameters (Figure 2).

According to our experimental results, the $CaAu_5$−$CaAu_4Bi$−$BiAu_2$ system exhibits two remarkable features. First, the terminal stoichiometric $CaAu_4Bi$ composition is evidently not stable; rather, Bi poorer (**I**−**IV**) or richer (**V**) phases always result; second and the more remarkable, *the five discrete homogeneity regions all exhibit the same crystallographic symmetry*. Therefore, the five phases in this system are not as simple as usually encountered. Looking back at textbook examples may help to understand the special phase relationships among these solid solution regions. As we know, a general phase diagram between solids A and B that are at most incompletely miscible may contain a solid solution of solute A in a matrix of B, a second with B as solute in A, and binary phases (nonstoichiometric or line compounds) within. In another case, A and B may form solid solutions at all concentrations if both have the same crystal structure, similar atomic radii, similar electronegativities, and similar valencies (Hume−Rothery rule). In either case, however, only one composition within a homogeneity range is available in a solid sample for a fixed set of reaction conditions (temperature, pressure, and composition). The $CaAu_5$−$CaAu_4Bi$−$BiAu_2$ system apparently presents a rare and different situation. Perhaps it might be better to treat **II**, **III**, and **IV** as intermediate phases between the two terminal solid solutions **I** and **V**, a situation that might seem comparable to many known systems. For example, the Mo−B binary system[33] contains not only two terminal solid solutions (of B in Mo and of Mo in B) but also four nonstoichiometric intermediate phases, Mo_2B, MoB, Mo_2B_5, and MoB_4. The Cu−Zn system[33] shows the same scenario: the so-called β-, γ-, η-brass phases exist as solid solutions in addition to the terminal α-brass. But, a major question would remain open as to why and how the intermediate phases (**II**, **III**, and **IV**) and the two terminal members (**I** and **V**) could all have exactly the same symmetry, in contrast to general observations that intermediate phases exhibit different crystal symmetries and structures as their compositions change. The last dilemma and the frequent occurrence of *pairs* of phases with similar dimensions as well are related to the uncommon phenomenon of spinodal decomposition. But before we give the evidence for these, the crystal and electronic structures will be considered, as these are also related to the driving forces for spinodal decomposition.

Crystal Structures. To uncover the structural differences between, and relationships among, the five nonstoichiometric phases, representative single crystals from three reactions were analyzed (Tables 2 and 3). Crystals **1** and **2** came from the same reaction, $x = 0.25$, and crystals **4** and **5**, from $y = 0.4$ (Table S1), as marked with bold numbers in Figure 1a. According to their single crystal X-ray structural analyses, all are isostructural ($F\bar{4}3m$, $MgCu_4Sn$-type[17]), with differences only in occupancies of the Wyckoff 4*a* and *4c* sites. These can also be viewed as substitutional derivatives of the $CaAu_5$ ($F\bar{4}3m$) and $BiAu_2$ (= $BiAu_4Bi$, $Fd\bar{3}m$) extremes. (The higher $Fd\bar{3}m$ symmetry arises for $BiAu_2$ because Bi occupies both 4-fold sites.) The most prominent feature of the ideal $CaAu_4Bi$, Figure 3, is a three-dimensional $_\infty^3[Au_4]$ network in which the relatively electropositive Ca and Bi alternately occupy the two independent 4*a* and *4c* sites, the centers of condensed truncated gold tetrahedra, to give the so-called Friauf polyhedra. Nearest neighbor distances in the whole family reported here increase markedly, with *d*(Au−Au) = 2.74−2.82 Å, *d*(Au−Ca/Au/Bi (4a, 4c)) a substantial 0.48 Å larger, and *d*(4a−4c) 0.14 Å still longer (Table S3). The 4-fold atom sets describe a zinc blende-type net that interpenetrates the $_\infty^3[Au_4]$ tetrahedral network, although bonding between them is relatively weak (below). The

(33) Massalski, T. B. *Binary Alloy Phase Diagrams*, 2nd ed.; Massalski, T. B., Ed.; ASM International: Materials Park, OH, 1990; Vol. 1.

Table 3. ICOHP Data for $CaAu_4Bi$ (eV)

Bond	Au-Au	Ca-Au	Bi-Au	Ca-Bi
Distance (Å)	2.793	3.275	3.276	3.421
bonds/cell	48	48	48	16
−ICOHP/bond (ave.)	1.40	0.38	0.54	0.35
−ICOHP/cell	67.2	18.24	25.92	5.6
Contribution (%)	57.5	15.6	22.2	4.8

differences among the three terminal compounds $CaAu_5$, $CaAu_4Bi$, and $BiAu_2$, Figure 1a, lie in the species filling alternating 4-fold sites: Ca and Au in Wyckoff 4*a* and 4*c* sites in $CaAu_5$, respectively, Bi in both sites in $BiAu_2$, and Ca and Bi in $CaAu_4Bi$, respectively.

Despite the fact that the elements Ca, Au, and Bi exhibit striking differences in terms of valence electrons, electronegativities, atomic radii, etc., all of them can to different degrees fill (and bond within) the Au_{12} network to yield stable compounds without a change in symmetry. This is a remarkable property of this system. However, larger differences in radii, valence electron counts, and electronegativities between M and Au result in rearrangements of this Au_4 network and degradation of the crystal symmetry. For example, MAu_5 (M = Sr, Ba, K, Rb, or Cs) exhibit hexagonal rather than cubic symmetry, with face-sharing of Au tetrahedra.[34] In other cases, chains or sheets of vertex-sharing Au_4 clusters separated by triel chains form in the presence of heavier triel (In or Tl) elements and other cations,[35] or puckered layers of such condensed Au_4 tetrahedra that are intergrown with open 4-bonded (Sn_4Au) regions in one case with tin.[36]

Electronic Structures. Figure 4 shows (a) the densities-of-states (DOS) and (b) the crystal orbital Hamilton populations (-COHP)[31,32] calculated for the ideal $CaAu_4Bi$. As can be seen, the Fermi energy (E_F) locates in a continuous band, characteristic of a metal and in agreement with resistivity measurements (below). As in other polar intermetallics, Au 5*d* states populate a broad energy range, ∼ −8.0 to −0.4 eV, with some extending above E_F; on the contrary, the Ca 3*d* states locate mainly above E_F, with only a few below that point. The Bi 6*s* states are very low, ∼3.0 eV below the lowest Bi 6*p* states. This situation resembles the behavior of trivalent Bi (e.g., in BiF_3), for which Bi $6s^2$ may be considered as an effective core. In contrast, the 6*s* and 6*p* states have a very small energy difference for pentavalent Bi (e.g., in BiF_5, Figure S2).

The -COHP data integrated to E_F (-ICOHP) for each pairwise interaction type in $CaAu_4Bi$ are given in Table 3 on both a per-bond and per-cell basis, whereas those for $CaAu_5$ and $BiAu_2$ are in Table S3. The average -ICOHP (Hamilton population) for Au−Au in $CaAu_4Bi$ is 1.40 eV/bond, three to four times those for Au−Bi (0.54), Ca−Au (0.38), and Ca−Bi (0.35). As might be expected, the total Au−Au population/bonding within the tetrahedral networks is dominant, whereas the other interactions are distinctly smaller. The last type of interactions (4a−4c) is down-rated on a per cell or molar basis because they occur only one-third as often in the structure. Thus the percentages of overall -ICOHP contributions per cell in $CaAu_4Bi$ are 57.5% from Au−Au bonding but ∼16 and 22% for Ca−Au and Bi−Au, respectively, and only ∼5% for Ca−Bi. Similar -ICOHP values and proportions are obtained for $CaAu_5$ and

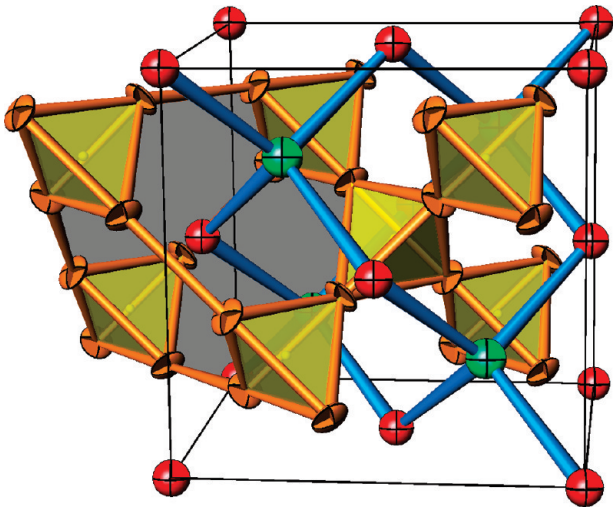

Figure 3. Perspective representation of the cubic structure of ideal $CaAu_4Bi$. Each Au_4 tetrahedron (golden) shares all of its corners with four other tetrahedra, generating a three-dimensional $_\infty^3[Au_{4/4}]$ tetrahedral network. The latter is interpenetrated by the ZnS-type network composed of Ca (red) and Bi (green) to generate Friauf polyhedra. Both Ca and Bi locate at the centers of truncated tetrahedra; one is shaded in gray.

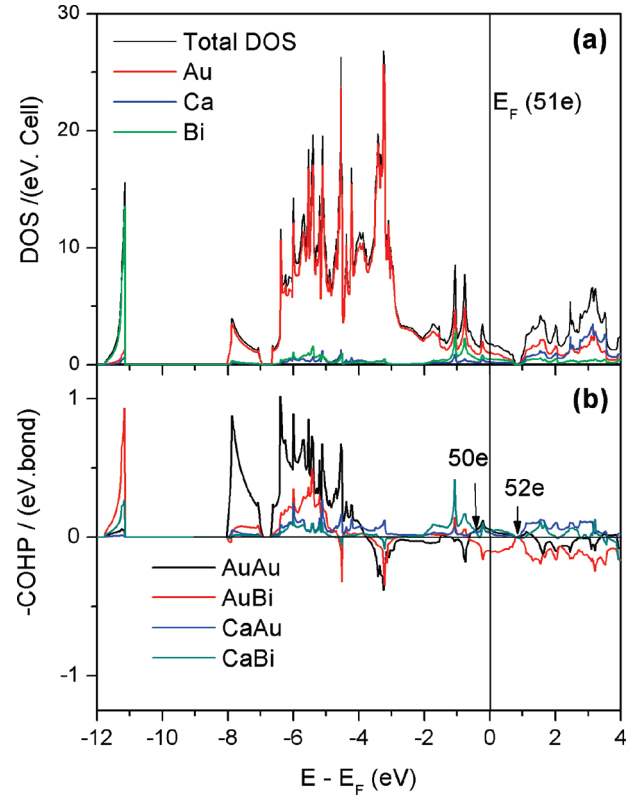

Figure 4. DOS and -COHP data for $CaAu_4Bi$. The marked *vec* values are per formula unit.

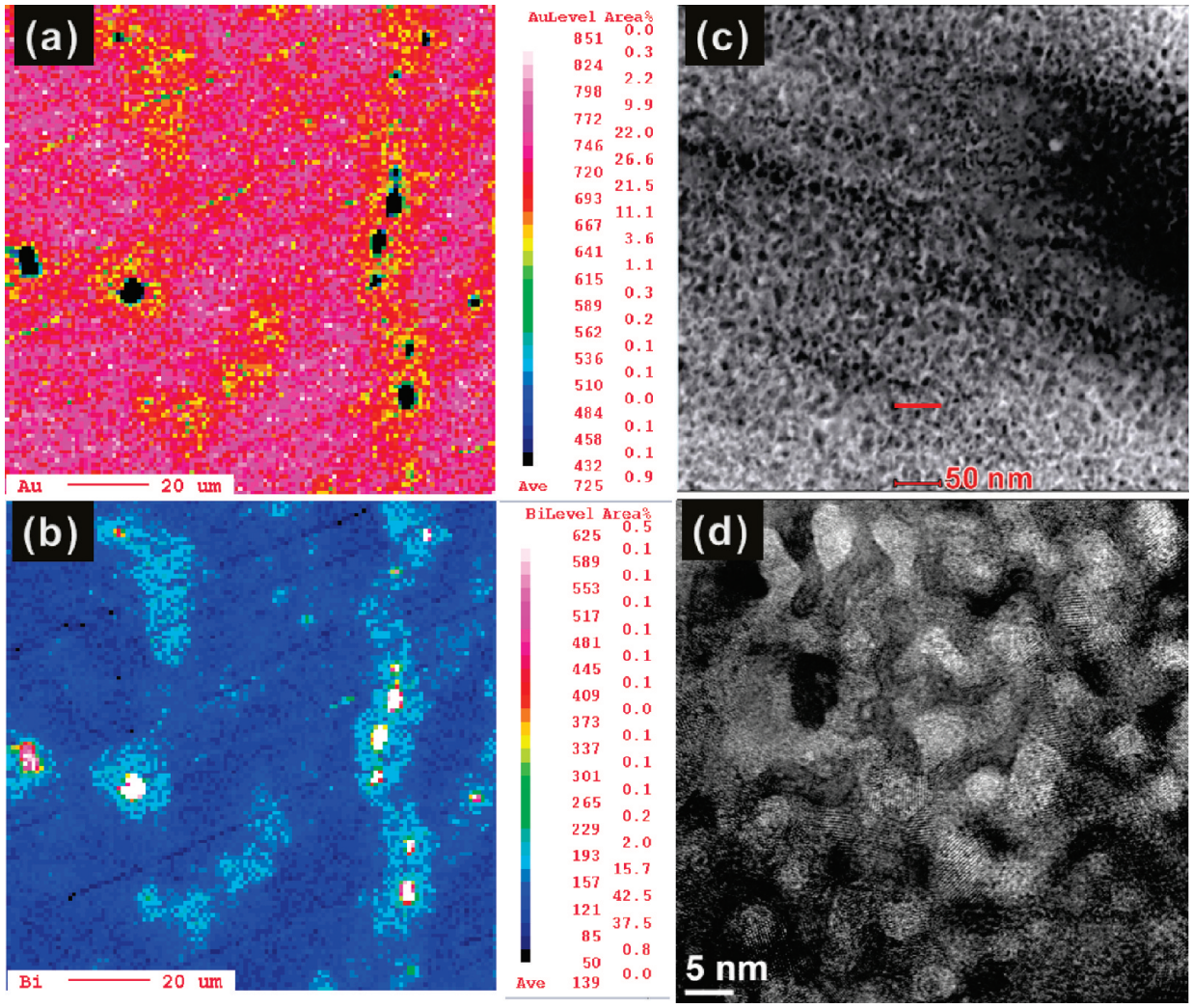

Figure 5. Contour maps of electron counts of (a) Au and (b) Bi on the same 100 × 100 μm^2 area of a nominal $CaAu_{4.25}Bi_{0.75}$ sample that was melted at 850 °C for 24 h, quenched in water, and then annealed at 400 °C for 1 week. The small black areas in (a) and white regions in (b) are Bi inclusions. (c) An STEM-HAADF image and (d) an HRTEM image for the same sample.

$BiAu_2$. All of these are consistent with the structural analyses showing that the Au_4 tetrahedral networks contribute the greatest bond populations regardless of whether Ca, Au, Bi atoms or their mixtures occupy the Wyckoff 4*a* and 4*c* sites.

Another electronic feature of ideal $CaAu_4Bi$ is that the Au−Bi interactions show substantial antibonding character at E_F (*vec* = 51 e including Au d^{10}), but these are better optimized one electron lower (50 e) or higher at a pseudogap (52 e), Figure 4b. This small effect suggests that bonding in the stoichiometric $CaAu_4Bi$ might be optimized with one more or one fewer valence electron. Interestingly, all pairwise bonds in $CaAu_5$ and $BiAu_2$ exhibit bonding or nonbonding character at E_F except for a minute Bi−Bi antibonding effect in the latter (Figure S3). The results agree with (but do not necessarily support) the fact that the stoichiometric $CaAu_{\sim 4}Bi$ phase can be obtained only with 10−15% Au in the Bi 4*c* position according to structural refinements and EDS data (**3**). Whether such a small antibonding effect at E_F has any connection with the free energy change associated with its spinodal decomposition remains a question.

Spinodal Decomposition around $CaAu_4Bi$. Spinodal decomposition occurs when composition fluctuations are small in degree and large in extent (size), giving rise to two slightly different compositions with the same structure. As a result, the powder patterns for spinodal products often exhibit broadened peaks or satellite reflections ("side bands") along with the main reflections or finally develop into double peaks as the spinodal decomposition process proceeds and crystal nucleation and growth take place,[37] all because of the effects of small particle sizes on coherent X-ray scattering. The five nonstoichiometric and discontinuous phase regions found in the ternary $CaAu_5$−$CaAu_4Bi$−$BiAu_2$ system with similar compositions and the same structure type seem to meet the requirements to undergo spinodal decompositions in composition regions that lie between them, Figure 1a. The powder patterns in Figure 1b (and others not shown) suggest that spinodal decompositions occur at ∼400 °C over ∼1 week for substantially all of the intermediate compositions that lie in the phase fields between any two solution regions, **I** and **II**, **II** and **III**, **III** and **IV**, etc.

(34) Villars, P.; Calvert, L. D. *Pearson's Handbook of Crystallographic Data for Intermetallic Phases*, 2nd ed.; American Society of Metals: Materials Park, OH, 1991; Vol. 1.
(35) Li, B.; Kim, S.-J.; Miller, G. J.; Corbett, J. D. *Inorg. Chem.* **2009**, *48*, 6573.
(36) Li, B.; Kim, S.-J.; Miller, G. J.; Corbett, J. D. *Inorg. Chem.* **2009**, *48*, 11108.
(37) Hargreaves, M. E. *Acta Crystallogr.* **1951**, *4*, 301.

More evidence for spinodal decomposition was obtained from a representative product of the nominal $CaAu_{4.25}Bi_{0.75}$ reaction that falls between **II** and **III**, Figure 1a (green/blue). Figure 5 shows the electron emission maps of (a) Au (red) and (b) the lesser Bi (lighter blue) on the basis of EPMA data, (c) an HAADF image, and (d) a high-resolution TEM image using the STEM technique. Panels (a) and (b) suggest that regions with slightly different compositions are present on a 10−50 μm scale. The two compositions were determined to be $Ca_{1.00(1)}Au_{4.44(4)}Bi_{0.56(3)}$ and $Ca_{1.02(1)}Au_{4.14(4)}Bi_{0.84(5)}$ by EDS analyses of multiple 1 μm^2 regions, corresponding to the nearest boundaries of phases **II** and **III**. Further direct evidence for spinodal products is the small noodle-like regions with different contrasts in (c), the HAADF (STEM) image. As described in the Experimental Section, these high resolution images are sensitive to atomic number, the brighter areas representing larger average atomic numbers. Therefore, the darker regions in (c) correspond to the **III** boundary, and the brighter regions, to that for **II**. In contrast, the HRTEM image in (d) on a 10-fold finer scale has no relationship to elemental proportions. Although the contrast also shows noodle-like regions, the dark and bright images here are the results of complex factors, e.g., particle orientation, composition, diffraction, surface effects, etc. However, apparent nanoscale particles (~5−10 nm) are evident in the HRTEM image, with different orientations characteristic of spinodal systems. One should note that the EDS-EPMA contour maps (a, b) are not directly comparable to STEM-HAADF and HRTEM images (c, d), even though these are for products of the same reaction, because both the sample regions and the spatial resolutions for the two groups are different. The resolution for EPMA is ~0.5 μm (the size of the beam), which is "large" compared with that of the STEM-HAADF in (d), ~0.13 nm. Moreover, all the specimens came from samples that had been annealed at 400 °C for 1 week, during which nucleation and growth processes were evidently initiated following the initial spinodal decomposition. Numerous lattice fringes from ca. 30 to 100 nm overall crystallites can be seen superimposed on the initial spinodal motif under higher magnification (Figures S5, S6). This also accounts for the absence of line broadening in the X-ray powder patterns, Figure 1b, that would otherwise be expected for spinodal products.[37] The powder pattern of a quenched sample that had not been annealed and the resultant line broadening and shifting are shown in Figure 7c (inset).

Approximate compositional boundaries between the individual nonstoichiometric regions and the intervening spinodal region can be fitted with the aid of EDS measurements or refined single crystal compositions for biphasic systems (given sufficient elemental proportions). A tutorial type result for the temperature−composition relationships are shown at the bottom in Figure 6 for the $CaAu_4(Au_{1-m}Bi_m)$ spinodal region over the $0.64 < m < 0.85$ range, together with a sketch of the corresponding free energy variations at the top. (Curves in other composition ranges were not developed because temperature dependent data had not been measured.) The upper consolute temperature was fitted to ~800 °C, in accord with the DTA results (below). The miscibility gap (red curve) is extrapolated to be symmetrical at ~70.6 at. % Au, corresponding to $CaAu_{4.24}Bi_{0.76}$ ($m = 0.76$). Accordingly, if a homogeneous alloy with this composition is heated at a high temperature (>800 °C) and then quenched to a lower temperature, e.g. 400 °C, the composition will initially be the same everywhere and its free energy will be near the maximum of the top curve (black). However, this alloy lies in the unstable (yellow) region, and small fluctuations in composition will (with the right ΔG relationships) produce Au-rich (to the right) and Bi-rich (to the left) spinodal growths on a very small length scale so as to decrease the total free energy. On top of this, some nucleation and conventional crystal growth will eventually occur in selected areas on some time scale until the equilibrium compositions α and β are reached. In the present system, most samples were annealed at 400 °C for 1 week. This statement is actually confirmed by the powder pattern of $CaAu_{4.25}Bi_{0.75}$ (Figure 1b), which lies very close to the spinodal center ($m = 0.76$, Figure 6). As shown in the former, this composition yields nearly equal volume fractions of **II** and **III** at their nearest boundaries, consistent with the phase rule. (Here **II** corresponds to the Bi-richer phase α, **III**, to the Au-richer β.)

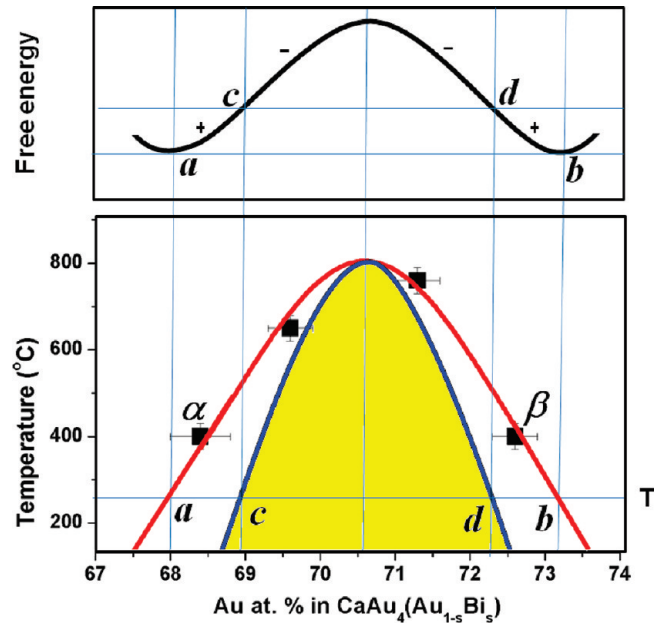

Figure 6. Bottom: the fitted phase boundary for $CaAu_{4.24}Bi_{0.76}$ (red) and the sketched curve for chemical spinodal decomposition (blue). Above the red line, the compositions are homogeneous and the system is stable. The region between red and blue lines is a metastable region. Samples with compositions in this region are stable to small fluctuations but unstable to large fluctuations, thus following the nucleation and growth mechanism. Samples below the blue line are unstable (yellow shaded area) and follow a spinodal decomposition mechanism without activation to yield a two-phase system. The top plot sketches the corresponding free energy−composition profile, with the signs of the second derivatives marked.

Spinodal pairs were also found for nominal $CaAu_4Bi$ samples (66.7 at. % Au, Figure 1b), outside of the simulated spinodal region in Figure 6 because the ideal phase is evidently unstable, separating liquid Bi and leaving a lower Bi (and higher Au) proportion in the bulk, as indicated by powder patterns. However, when more Bi is present, spinodal decomposition may no longer occur, and only the **III** (the β) phase appears, e.g., for $CaAu_{3.5}Bi_{1.5}$ (58.3% Au), Figure S1.

Phase Stability, Susceptibility, and Resistivity. Figure 7 shows the DTA results for nominal $CaAu_4Bi$ (a) and $CaAu_{4.25}Bi_{0.75}$ (b) together with insets of the XRD patterns before and after. As mentioned before, both $CaAu_4Bi$ and $CaAu_{4.25}Bi_{0.75}$ are subject to spinodal decomposition into α (Au-rich) and β (Bi-rich) pairs, which for simplicity stand for all compositions in the range between **II** and **III** in the following context. On heating, the DTA curve of $CaAu_4Bi$ exhibits two endothermic peaks at ~717 and ~808 °C; on cooling, the corresponding

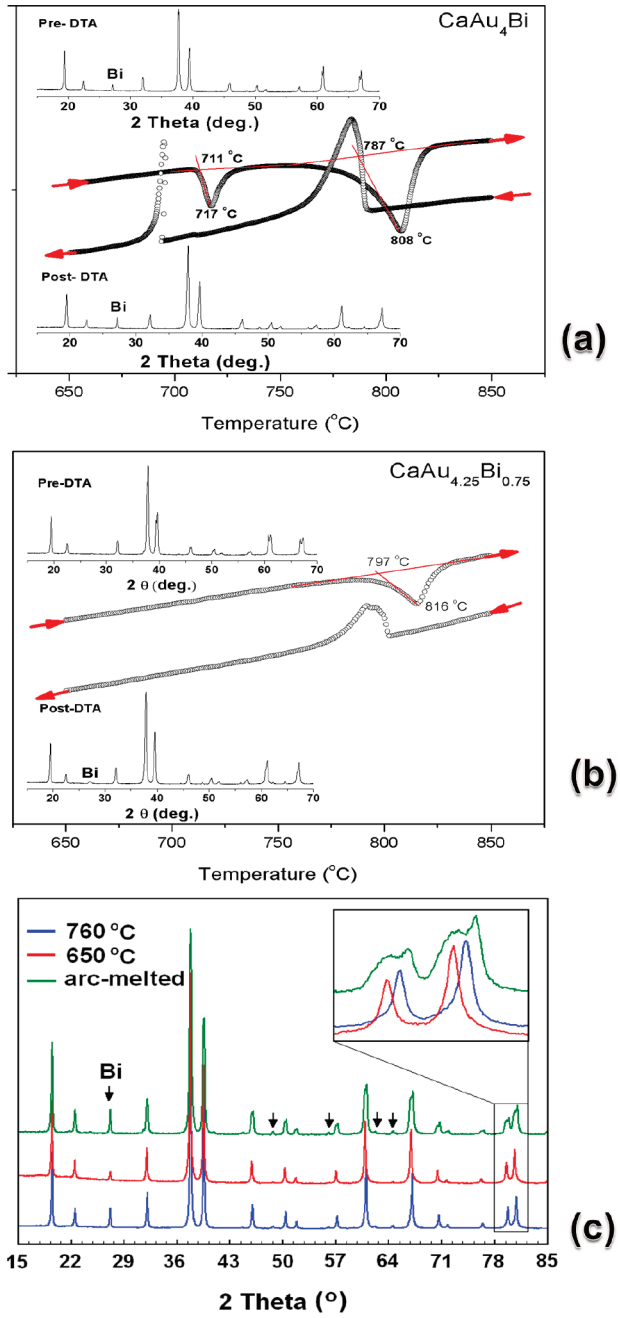

Figure 7. Heating and cooling DTA curves for (a) $CaAu_4Bi$ and (b) $CaAu_{4.25}Bi_{0.75}$, together with powder patterns before and after DTA scans. (c) Three powder patterns of $CaAu_4Bi$ as arc-melted and as separately annealed at 650 and 760 °C, respectively. For comparison, a small region of these powder patterns is shown in the inset vertically displaced to show variations of peak positions and line widths.

exothermic peaks reappear, but now at lower temperatures because of supercooling. However, the two temperatures do not represent the separate fusion/solidification of α and β (or of β and α); rather, the melting points for both α and β are ~808 °C. (Actually, melting points of α and β are not exactly the same, as suggested by the long pretail of the endothermic peak at 808 °C.) As for the peak at 717 °C, it corresponds to the reversible peritectic reaction of α (s) + Bi (*l*) ⇌ β (s). This is supported by the DTA curve of $CaAu_{4.25}Bi_{0.75}$, Figure 7b, in which the peak at ~717 °C disappears, because only a trace of Bi exists in the nominal $CaAu_{4.25}Bi_{0.75}$ product. In addition, XRD patterns of $CaAu_4Bi$ samples that had been separately annealed at 650 and 760 °C for a week and quenched in water also show that the endothermic peak at 717 °C should be assigned to a peritectic reaction, Figure 7c. The original arc-melted sample of $CaAu_4Bi$ contains both α and β phases plus some Bi, and after annealing at 760 °C, the β phase disappears, with Bi peak intensities showing a slight change. On the contrary, the α phase disappears on annealing at 650 °C, and simultaneously, peak intensities for Bi are much lower than those before annealing, suggesting that Bi is consumed in the phase transition at this temperature.

Some measurements of physical properties were included to look for possible differences for a spinodal pair. According to our susceptibility and resistivity data, Figure S6, α and β (from nominal $CaAu_4Bi$) are paramagnetic and poor metals. From the susceptibility data, the sample annealed at 760 °C (α) is more diamagnetic than that annealed at 650 °C (β), presumably because more diamagnetic Bi was present in the former (Figure 7c). The same holds for the resistivities, in which polycrystalline α shows the larger temperature-dependent resistivity. Nevertheless, both α and β data are not very sensitive to temperature; the calculated coefficients over 50−300 K are 0.057 uΩ·cm/K for α and 0.014 uΩ·cm/K for β.

Summary

The structures of $CaAu_5$, $BiAu_2$, and $CaAu_4Bi$ exhibit a common Au_4 tetrahedral host network, in which the polyhedral centers (4*a*, 4*c*) may be occupied by Ca, Au, or Bi, some in mixtures in ternary examples. Bonding analyses also reveal that Ca−Au, Bi−Au, and exo-Au−Au bonds in these products have lower total Hamilton populations (-ICOHP) relative to the major Au−Au interactions in the network and -ICOHP values for interactions between the 4*a*−4*c* atoms are particularly small. The Bi−Au interactions in an ideal $CaAu_4Bi$ model exhibit appreciable antibonding character around E_F. The multiple discrete nonstoichiometric phases around $CaAu_4Bi$ provide excellent structural bases and good opportunities to develop spinodal systems. Direct evidence for spinodal decomposition of $CaAu_{4.25}Bi_{0.75}$ is given by XRD, STEM, and EPMA data, this composition being close to the average of the spinodal pair. Spinodal decompositions evidently occur for all starting compositions that lie between the five discrete nonstoichiometric phases established by powder pattern data. However, it has not been our intent to study temperature- or time-dependent microstructure evolutions on this system, which can give much detailed information on spinodal decomposition or the thermodynamic processes for each spinodal region. As a case study, this investigation provides a useful lesson for the development of novel and complex spinodal systems on the basis of crystal structure and electronic structure properties. Future studies will be carried out with the aim to discover more spinodal systems via various substitutions based on $CaAu_4Bi$ and to evaluate their applications as potential thermoelectric materials.

Acknowledgment. The authors thank A. Kracher for collection and phase analyses of EDS data, Y. Wu for the STEM-HAADF and HRTEM images, K. Dennis for allowing use of the DTA Instruments, and N. Ni for magnetic and resistivity measurements. These measurements were all vital to the present study. This research was supported by the Office of the Basic Energy Sciences, Materials Sciences Division, U.S. Department of Energy (DOE) and was carried out in the facilities of the Ames Laboratory. The Ames Laboratory is operated for the DOE by Iowa State University under Contract No. DE-AC02-07CH11358.

Supporting Information Available: CIF outputs; list of reactions and refined lattice parameters (Table S1); important interatomic distances (Table S2); -ICOHP data (Table S3); XRD patterns for $Ca_{1.4}Au_4Bi_{0.6}$ and $CaAu_{3.5}Bi_{1.5}$ (Figure S1); calculated electronic structures of BiF_3 and BiF_5 (Figure S2) and of $CaAu_5$ and $BiAu_2$ (Figure S3); microprobe analysis maps of $CaAu_4Bi$ (Figure S4); more HRTEM images of $CaAu_{4.25}Bi_{0.75}$ (Figures S5, S6); magnetic and susceptibility data for $CaAu_4Bi$ annealed at 650 and 760 °C (Figure S7). These materials are available free of charge via the Internet at http://pubs.acs.org.

JA100250D